electronics

MDPI

Article

A Line Selection Method for Small-Current Grounding Faults Based on Time–Frequency Graphs and Image Detection

Lei Li, Shuai Hao * and Weili Wu

College of Electrical and Control Engineering, Xi'an University of Science and Technology, Xi'an 710054, China; liqieru@xust.edu.cn (L.L.); wwllxm1999@xust.edu.cn (W.W.)
* Correspondence: haoxust@xust.edu.cn

Abstract

Aiming at the problem that the multi-scale feature interaction ability of the traditional deep learning-based line selection algorithm is insufficient, resulting in the decline of line selection accuracy, a multi-scale feature fusion line selection method based on transfer learning is proposed, abbreviated as TLM-Net. Firstly, to address the issue of the insufficient generalization ability of the line selection network in small-sample scenarios, a simulation data pre-training framework is constructed, and a robust feature representation basis is established through a cross-domain knowledge transfer mechanism. Secondly, aiming at the problem of insufficient extraction of feature information by traditional algorithms, a multi-scale feature fusion network (MFFN) is designed to integrate global context information and local detail features, achieving cross-level semantic complementarity and spatial alignment optimization. Then, to enhance the representation ability of weak fault feature information, an EKA mechanism integrating variable kernel convolution is designed. The background interference is reduced through adaptive multi-region feature focusing, and the edge recognition accuracy of the model for irregular targets is improved. Finally, the pre-trained model is transferred to the target domain by adopting the transfer learning strategy, and the network parameters are fine-tuned in combination with the on-site data to achieve cross-domain adaptation of the feature space. The experimental results show that the TLM-Net algorithm's mAP@0.5 reaches 98.5%, the accuracy rate and recall rate reach 98.3% and 96.5%, respectively, and the accuracy is improved by 37.5% compared with the original model.

Keywords: fault line selection; deep learning; small sample; transfer learning; multi-scale feature fusion

Check for updates

Academic Editor: Francisco Javier Ruiz-Rodríguez

Received: 4 February 2026
Revised: 10 March 2026
Accepted: 10 March 2026
Published: 11 March 2026

Copyright: © 2026 by the authors. Licensee MDPI, Basel, Switzerland. This article is an open access article distributed under the terms and conditions of the Creative Commons Attribution (CC BY) license.

1. Introduction

Medium- and low-voltage distribution networks are the key links connecting power grids and end users, and their safe and stable operation is crucial to the reliability of power supply systems. Single-phase grounding faults are the most frequent faults in small-current grounding systems, and accurate and rapid fault line selection is the primary premise for fault handling and power restoration. However, the small fault current, weak fault characteristics and scarcity of on-site fault samples in such systems bring great challenges to traditional line selection methods. In recent years, deep learning-based image detection technology has shown great potential in extracting subtle fault features, but its application in small-current grounding fault line selection is limited by insufficient multi-scale feature fusion and poor generalization ability under small samples. To address the above key

technical problems, this paper proposes a TLM-Net fault line selection method based on transfer learning, time–frequency graph conversion and multi-scale feature fusion.

1.1. Research Significance and Practical Demands

In China, medium- and low-voltage distribution networks generally adopt the small-current grounding method, which is divided into the neutral point grounded through a high-resistance system, the neutral point grounded through an arc-suppression coil system and the neutral point ungrounded system [1]. In an actual operation system, single-phase grounding faults account for more than 80% of the overall fault statistics [2]. Their inducing mechanisms show significant multi-source characteristics. Factors such as insulation damage of distribution lines, lightning strike overvoltage, single-phase tree line faults, and equipment aging can all lead to single-phase grounding.

In a small-current grounded operation system, if a single-phase grounding anomaly occurs, the symmetry of the system line voltage still exists, and the fault current is relatively small. Usually, the power-off protection action will not be triggered immediately [3–5]. However, the voltage of the non-faulty phase will rise. If effective measures are not taken, it may cause insulation failure, and, in extreme cases, even induce regional power supply interruption [6]. Although this system has a high power supply reliability, the smaller fault current also increases the difficulty of fault line selection. Efficient and precise selection technology is the prerequisite for maintaining the reliability of power supply.

1.2. Literature Review

Small-current grounding fault line selection is a key technical problem in the operation and maintenance of medium- and low-voltage distribution networks, and a large number of research results have been formed by scholars at home and abroad. According to the different fault characteristic quantities and analysis methods, the existing line selection methods can be divided into three categories: steady-state signal-based methods, transient signal-based methods and artificial intelligence-based methods [7–9].

1.2.1. Steady-State Signal-Based Methods

This type of method takes the steady-state electrical parameters of the system after a fault as the core characteristic quantity, and realizes fault line selection by extracting the differences in the zero-sequence current amplitude, phase, harmonic component and active power between each line. Wang et al. [10] proposed a fault line selection method based on the phase comparison of the fault phase voltage and zero-sequence current. Line selection is achieved by constructing the phase relationship between the two. However, due to the forced resonance compensation mechanism of the NES, the inductive current injected into the arc-suppression coil forms an active compensation effect of amplitude matching and phase cancelation with the capacitive current, resulting in the amplitude of the zero-sequence current in the faulty line being canceled out by the compensation current vector. Its phase offset characteristics also tend to be blurred due to the dominance of inductive current components, making it difficult to determine the faulty line under the traditional phase comparison criterion.

1.2.2. Transient Signal-Based Methods

Transient signals have the advantage of joint analysis in the time–frequency domain. For instance, the wavefront steepness can be extracted through wavelet transform, and the eigenmode function can be analyzed by the Hilbert–Huang transform. Through these time–frequency analysis methods, multi-dimensional fault feature vectors can be constructed. Therefore, in-depth research on the feature extraction and analysis of zero-sequence current transient components can improve accuracy. Jiang al. [11] proposed a line

selection method that combines traveling wave line selection with transient signals. Experiments have proven that it can solve the issue of low line selection reliability. However, Li et al. [12] pointed out that the use of transient signals may be affected by objective factors, such as the time of fault occurrence, grounding resistance, and equipment sampling performance, resulting in unclear or unstable transient characteristics during line selection, and subsequently leading to problems such as reduced line selection sensitivity and reliability.

1.2.3. Artificial Intelligence-Based Methods

Deep feature learning models based on artificial neural network architectures have demonstrated powerful pattern recognition capabilities for complex power systems with weak fault features during end-to-end training on large-scale labeled datasets. Especially in small-current grounding systems, this technology, through a multimodal feature fusion strategy, can effectively extract fault features containing non-stationary transient components and achieve fault line selection. Su et al. [13] proposed a novel AdaBoost-based single-phase earth ground fault identification model is put forward. By depicting the zero-sequence circuit of the power distribution system, a feature is constructed that can reflect the local and global evolution processes during faults. Cheng et al. [14] proposed a method of constructing a three-dimensional spatial domain image of a three-phase current, projecting it to different planes, respectively, fusing them, and finally using a target detection algorithm to achieve fault line selection. Under the influence of multiple factors, such as the lack of manual extraction of fault feature information, compared with traditional methods, the fault identification strategy based on image feature extraction shows significant technical advantages in three dimensions: modal separability, algorithm decision confidence, and noise suppression ability.

However, the accuracy of algorithms based on deep learning depends on a large number of data samples, which has a huge impact on the accuracy of object recognition. Transfer learning pre-trains network models by leveraging historical data and incomplete data. This can be transferred to a new model, enabling high-precision detection of targets under small-sample conditions. To this end, a novel line selection method based on transfer learning is proposed.

1.3. Main Contributions

This paper proposes a TLM-Net-based fault line selection method for small-current grounding systems, which effectively solves the problems of low accuracy, poor generalization ability and weak feature recognition in traditional line selection algorithms. The main innovative contributions of this work are summarized as follows:

(1) A transfer learning-based pre-training framework for small-sample scenarios. A simulation data pre-training mechanism is constructed to make up for the scarcity of real on-site fault samples. By means of cross-domain knowledge transfer from the source domain (simulation data) to the target domain (on-site data), the generalization ability of the line selection model and the robustness under small-sample conditions are significantly improved.

(2) A multi-scale feature fusion network (MFFN) for global–local feature synergy. Aiming at the insufficient multi-scale feature interaction of the traditional FPN + PAN architecture, the MFFN is designed with a three-branch structure, which realizes the effective integration of global context information and local detail features of fault time–frequency graphs, and achieves cross-level semantic complementarity and spatial alignment optimization of features.

(3) An improved EKA mechanism fusing alterable kernel convolution (AKConv). Based on the EMA module, the AKConv is integrated to construct the EKA mechanism,

which realizes adaptive multi-region feature focusing to suppress background noise interference, and flexibly adjust the convolution kernel shape/parameters to improve the model's edge recognition accuracy for irregular fault feature targets.

(4) A high-precision line selection scheme integrating time–frequency transformation and image detection. The one-dimensional zero-sequence current signal is converted into two-dimensional time–frequency graphs by wavelet transform, which solves the problem of unobvious feature distinction of original signals. Combined with the improved target detection network, the fault line selection is transformed into an image feature recognition task, which effectively improves the detection accuracy and interpretability of the line selection algorithm.

Section 2 details the design of the TLM-Net model and its key modules; Section 3 presents the experimental setup and results analysis; and Section 4 draws the main conclusions of this study.

2. Fault Line Selection Method Based on TLM-Net

Based on the idea of transfer learning, a novel method TLM-Net is proposed to improve the line selection accuracy under small-sample conditions. The algorithm framework is shown in Figure 1.

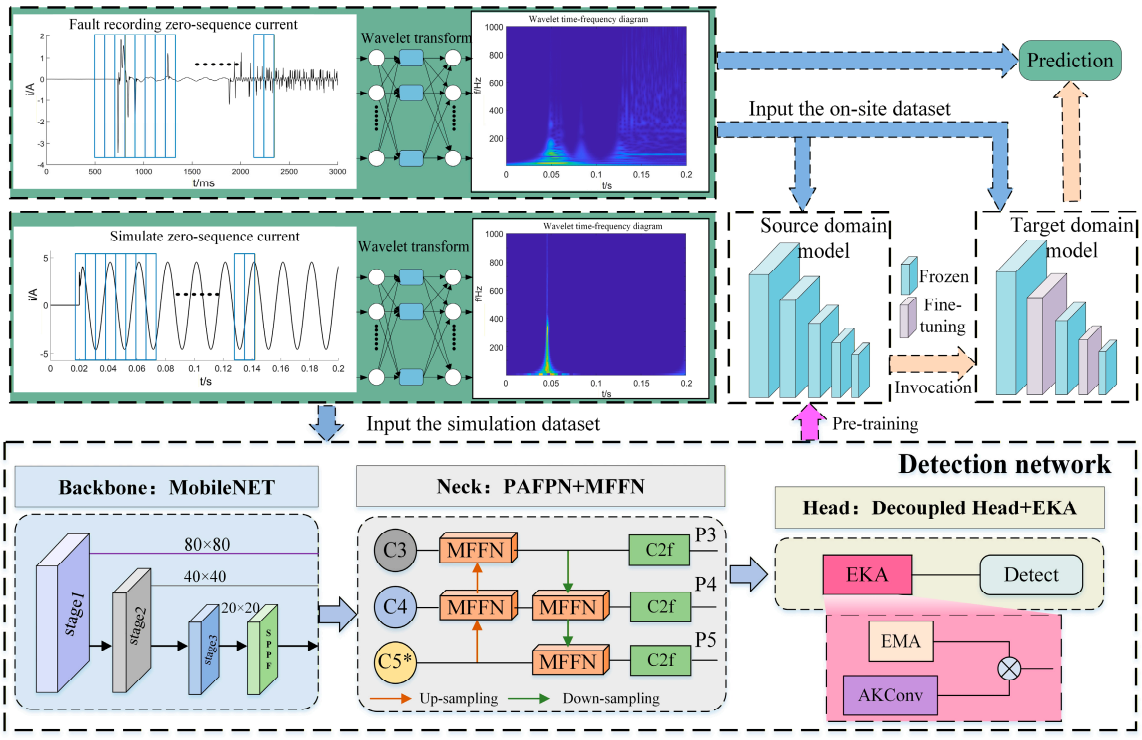


Figure 1. TLM-Net network structure.

The detection process of the TLM-Net line selection algorithm is as follows:

(1) By setting different fault parameters, the simulated data is obtained, which is mapped into a two-dimensional time–frequency graph through wavelet transform.

(2) The simulation data is input into the designed network to obtain a pre-trained model, which can learn the prior knowledge of the fault image.

(3) Aiming at the drawback of weak feature comparison in the field data of small-current line selection, the MFFN (multi-scale feature fixed network), which integrates global information and local information, is utilized to obtain more abundant and comprehensive feature information in the dataset.

(4) To reduce the influence of background noise during line selection on data with high similarity, the EKA (efficient multi-scale and alterable kernel convolution attention) mechanism is utilized. The feature recognition ability of the line selection network is enhanced to better detect the target and improve the saliency of the target area.
(5) Input the on-site data into the improved network and train it with the pre-trained model to obtain the target domain model, and then test and verify it with the on-site data.

2.1. Data Processing Based on Wavelet Transform

Wavelet transform can conduct detailed analysis of signals through operations such as scaling and translation [15]. To concretely represent the data difference between faulty lines and non-faulty lines, the method of wavelet transform is selected to extract the high-frequency information contained in the zero-sequence current and reconstruct the one-dimensional data into a two-dimensional time–frequency graph.

Let the zero-sequence current be $f(t)$, and after continuous wavelet transform, it can be expressed as follows:

$$W_\Psi(a,b) = \int_{-\infty}^{+\infty} f(t)\Psi_{a,b}(t)dt \quad (1)$$

$$\Psi_{a,b}(t) = \frac{1}{\sqrt{a}}\Psi_{a,b}\left(\frac{t-b}{a}\right) \quad (2)$$

In Equations (1) and (2), a is the expansion factor; b is the translation factor; $\Psi_{a,b}(t)$ is the wavelet coefficient; and t is the time variable. Continuous wavelet transform includes the following processes:

Let C_i be a wavelet sequence:

$$C_i = 2F_c \cdot L \quad (3)$$

In Equation (3), L represents the length of the scale sequence. Let the wavelet scale be denoted by S:

$$S = C_i / L \quad (4)$$

The actual frequency of the wavelet is as follows:

$$F_a = F_s \cdot F_c / S \quad (5)$$

In Equation (5), F_a is the actual frequency of the wavelet, F_s is the sampling frequency, and F_c is the center frequency.

The continuous wavelet transform (CWT) is adopted to convert the one- dimensional zero-sequence current time-domain signal into a two-dimensional time–frequency graph, and all key parameters are strictly optimized for the characteristics of small-current grounding fault signals (low amplitude, low frequency < 400 Hz, and transient duration 0~0.2 s). The detailed parameter specifications are as shown in Table 1:

Table 1. Parameter settings during the wavelet transformation process.

Parameter Category	Specific Parameters
Signal Acquisition	Sampling rate: 1000 Hz Window length: 0.2 s (200 sampling points)
Wavelet Basis Function	Mother wavelet: Morlet wavelet
Scale Setting	Number of scales: 64 scales
Scale-to-frequency mapping	$f = (f_c \cdot f_s)/s\sqrt{2}$
Normalization	Pre-transform normalization: Z-score normalization Post-transform normalization: Min–max normalization

2.2. Multi-Scale Feature Fusion Network

The FPN + PAN architecture, which is widely used in the existing object detection framework, adopts a fusion method of directly summing after scale alignment when dealing with multi-scale input features. This simple superposition operation may lead to the incomplete exploration of semantic complementarity between features at different levels, resulting in the problem of a limited cross-scale feature fusion effect. Therefore, this paper proposes an MFFN model, as shown in Figure 2.

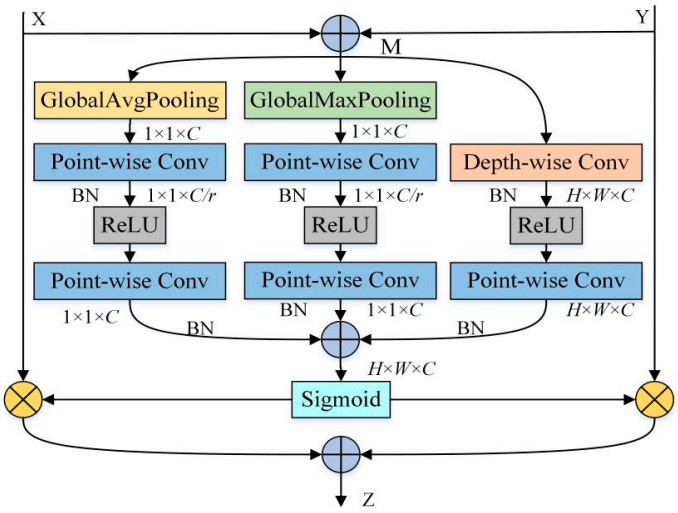


Figure 2. MFFN model structure.

As shown in Figure 2, let the dimensions of the X and Y input feature maps be $H \times W \times C$. The MFFN module performs three differentiation processes on the input features. The first two branches perform global average pooling and global max pooling operations, respectively, on each channel in the fused feature layer to streamline the channel's information and generate a new $1 \times 1 \times C$ feature layer. Subsequently, through two-dot convolution operations, the feature layer $1 \times 1 \times C$ is first compressed to a smaller dimension $1 \times 1 \times C/r$, and then the number of output channels is expanded to C by using the dot convolution operation of C convolution kernels, thereby achieving the effective fusion of channel information. During this process, batch normalization technology is introduced to optimize the model's performance.

In the third branch of the MFFN, depth-separable convolution is adopted. This path first performs a hierarchical convolution operation on the input fusion feature layer, selects a 3×3 convolution kernel, and sets the step size to 1. Immediately after, the feature expression ability is enhanced through normalization processing and the ReLU activation function. Then, element-by-element convolution is performed, using a 1×1 convolution kernel with the step size also set to 1. This series of hierarchical and point-by-point convolution steps ensures that the size of the feature map and the number of channels remain unchanged. Ultimately, the feature maps generated by the three paths are superimposed and processed through the Sigmoid activation function to obtain the updated feature map weights. The calculation formulas for the MFFN module are as follows:

$$F_1 = \mathrm{BN}(\mathrm{PWConv}(\delta(\mathrm{BN}(\mathrm{PWConv}(\mathrm{AvgPool}(\mathrm{M})))))) \tag{6}$$

$$F_2 = \mathrm{BN}(\mathrm{PWConv}(\delta(\mathrm{BN}(\mathrm{PWConv}(\mathrm{MaxPool}(\mathrm{M})))))) \tag{7}$$

$$F_3 = \mathrm{BN}(\mathrm{PWConv}(\delta(\mathrm{BN}(\mathrm{DWConv}(\mathrm{M}))))) \tag{8}$$

$$F_4 = F_1 + F_2 + F_3 \tag{9}$$

$$Z = (\sigma(F_4) \times X) + (\sigma(F_4) \times Y) \tag{10}$$

In Equations (6)–(10), X and Y are features that need to be fused; M is the initial feature; Z is the feature map output by the MFFN module; F_1 and F_2 represent the outputs of the first two branches; F_3 represents the output of the third branch; $\sigma(\bullet)$ represents the Sigmoid; $\delta(\bullet)$ represents the ReLU; and BN is batch normalization.

2.3. EKA Mechanism

To address the issue that some on-site data feature information is weak and vulnerable to noise interference, this chapter is based on the EMA (Efficient Multi-Scale Attention) model [16]. An improved EKA model incorporating fused variable kernel convolution, AKConv (alterable kernel convolution) [17] is proposed, as shown in Figure 3.

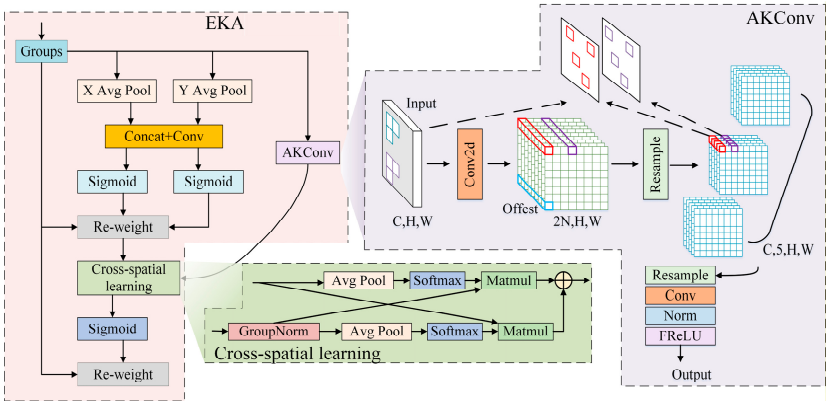


Figure 3. EKA mechanism.

2.3.1. EMA Mechanism

As shown in Figure 4, EMA achieves deep network optimization through a multi-branch parallel architecture while maintaining the information integrity of all channels without reducing their dimensions.

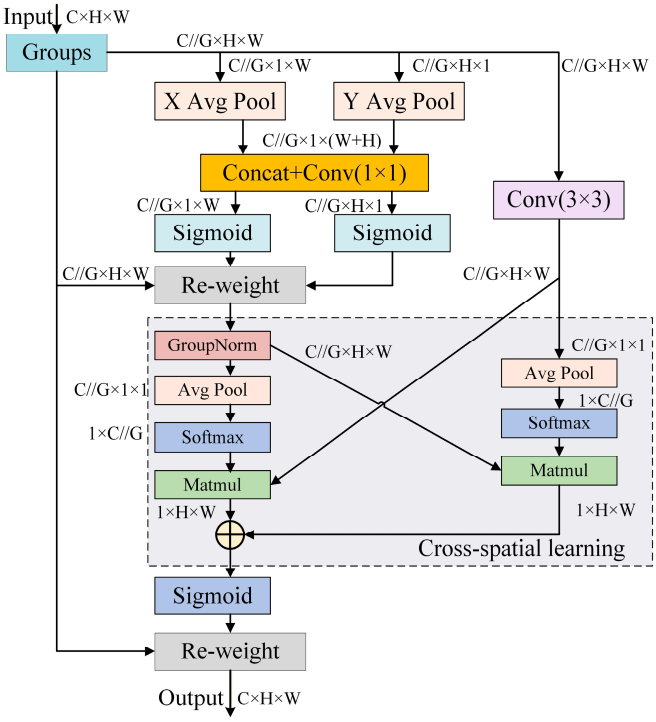


Figure 4. EMA mechanism.

For EMA, the data is first grouped and then processed through three paths: two paths first use 1×1 convolution combined with one-dimensional global average pooling, while the other deepens feature extraction through 3×3 convolution. The output features of these two paths are fused after being activated and normalized by Sigmoid, aiming to capture pixel-level paired relationships. EMA adopts a cross-spatial dimension feature aggregation mechanism. It extracts the global spatial context information output by the convolutional path through a two-dimensional pooling operation and performs dimension alignment processing on the channel features of the parallel sub-network branches. On this basis, EMA applies the SoftMax function to perform linear transformation fitting on the output of 2D pooling. Ultimately, through the dot-product operation of the matrix, the results of parallel processing are synthesized to generate the first spatial attention map.

2.3.2. Alterable Kernel Convolution

Due to the fact that, in the line selection dataset, the differences between faulty lines and non-faulty lines are not obvious enough, and the edges of their feature regions are irregular, in response to this issue, AKConv is introduced into the EMA mechanism.

In the architecture of convolutional neural networks, the sampling mesh of standard convolution has a predefined fixed geometric structure. This fixed structure enables it to only capture local neighborhood features and lacks the ability to capture the correlation information of distant positions in the image. However, detachable convolution can flexibly adjust the sampling mesh by introducing learning-type offsets, which to a certain extent alleviate this limitation. However, whether it is standard convolution or deformable convolution, they both rely on regular sampling meshes and do not support convolution kernels with any number of parameters. In addition, as the size of the convolution kernel increases, the number of required convolution parameters will increase sharply, showing square-level growth, which poses a higher demand on hardware resources. AKConv can arbitrarily change the number of convolution kernels, avoiding an excessive number of model parameters. The AKConv structure is shown in Figure 5.

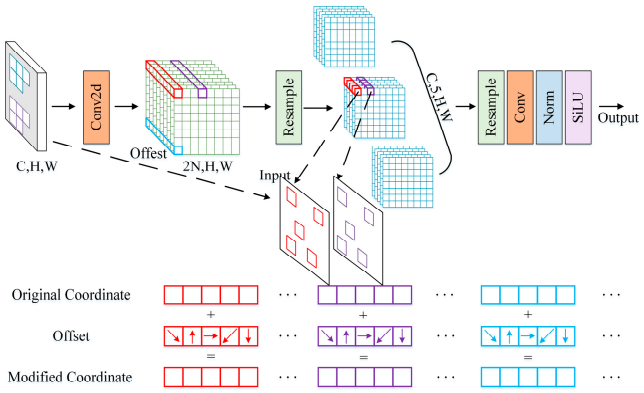


Figure 5. AKConv structure.

Similar to deformable convolution, in AKConv, the offset of the corresponding convolution kernel is first obtained through convolution operations, with dimensions of B, 2N, H, and W, where N is the size of the convolution kernel. Then, the modified coordinate $(P_0 + P_n)$ is obtained by adding the offset to the original coordinate. Finally, the features at the corresponding positions are obtained through interpolation, resampling and shape readjustment.

As shown in Figure 6, the convolution kernel parameters of variable kernel convolution are not fixed and can be of any number.

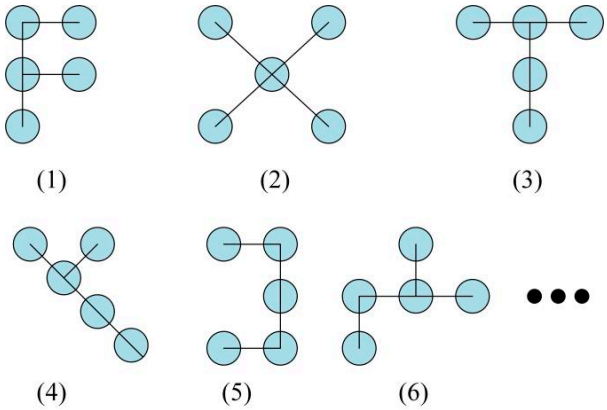
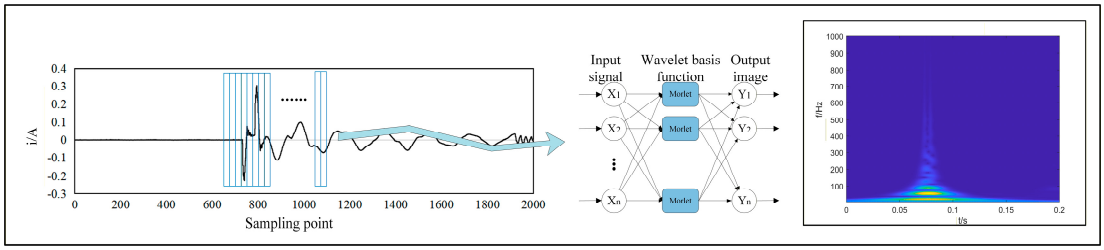


Figure 6. AKConv kernel shape.

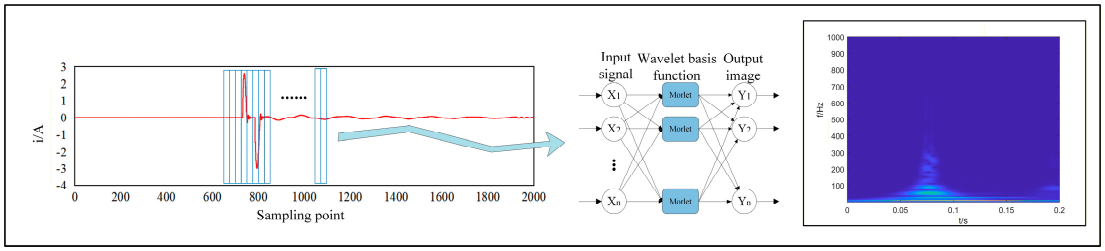
2.4. Dataset Preparation

2.4.1. On-Site Measured Data

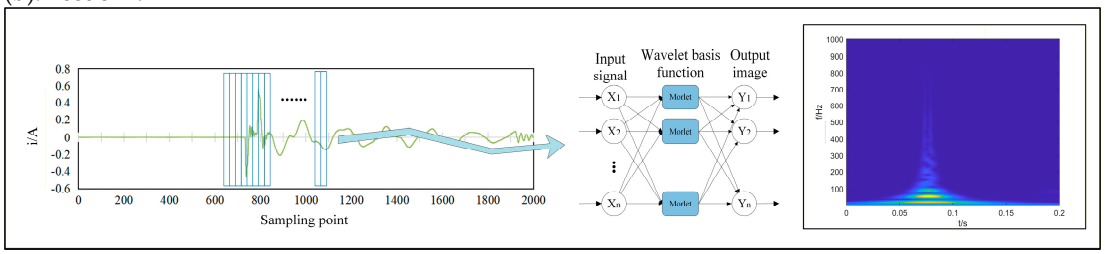
As shown in Figure 7, the on-site data is mapped into a two-dimensional image by using the wavelet transform, which can concretely represent the feature differences between different lines, and reduce the information interference of external factors on the original data.



(**a**). Feeder 1.



(**b**). Feeder 2.



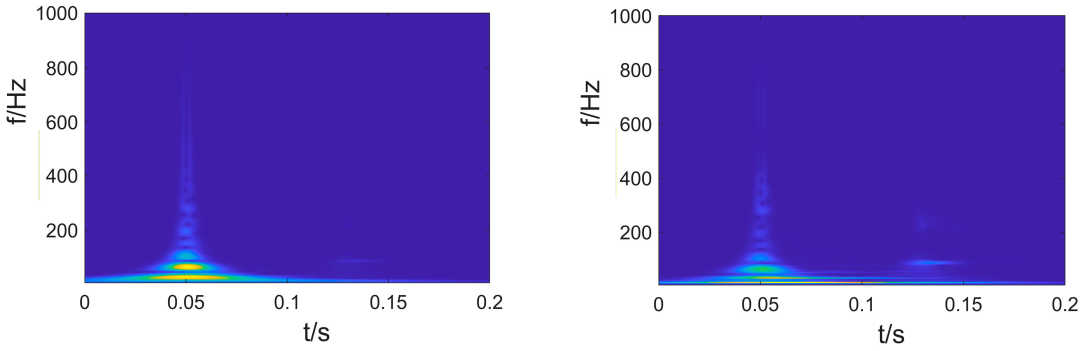
(**c**). Feeder 3.

Figure 7. Zero-sequence current of each feeder and its wavelet transform under single-phase grounding fault.

From Figure 7, the recorded waveform data of a single-phase grounding fault in feeder 2 of a 10 kV distribution network with a neutral point non-effectively grounded system is shown. Analyzing this waveform data, although there are differences in phase and amplitude between feeder 2 and the other lines, the above waveform diagram is presented after magnification processing. Under the same coordinate system, there is still

the drawback there not being an obvious comparison. For the modal aliasing defect of one-dimensional time-domain waveforms, time–frequency analysis technology can precisely distinguish between faulty circuits and non-faulty circuits.

The field data adopted in the experiment is the real fault recording wave data of a certain substation. After wavelet transform, 1800 time–frequency graphs can be obtained, as shown in Figure 8.



(**a**) Non-faulty lines (**b**) Faulty lines

Figure 8. Time–frequency diagram of on-site data sample.

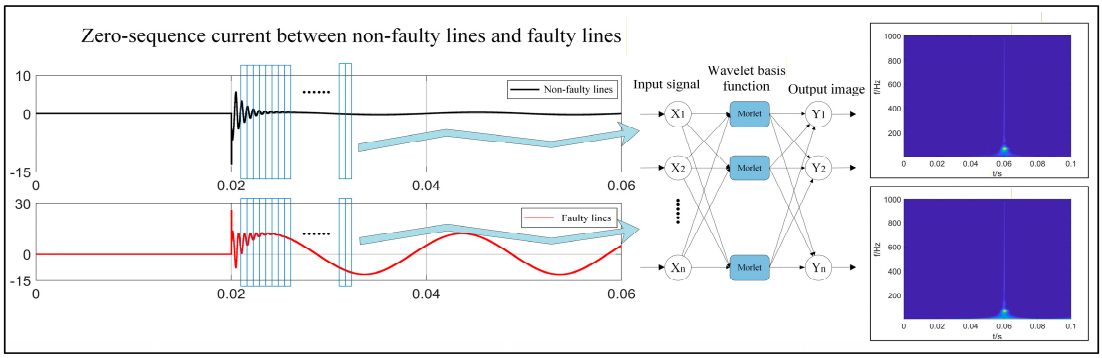
2.4.2. Simulation Data

The simulated zero-sequence current data is obtained by setting different parameters, such as the location of the fault point, the initial phase of the fault, and the grounding resistance. In Figure 9, when the grounding resistances are 10 Ω, 100 Ω, and 300 Ω, respectively, the time–frequency diagram changes. As the grounding resistance increases, the transient process exhibited by the zero-sequence current shortens, and the zero-sequence current in both the faulty and non-faulty lines decreases.

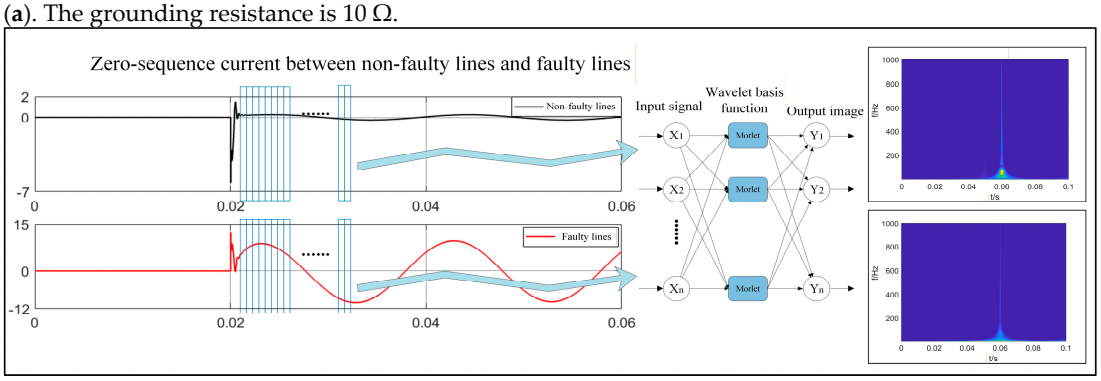
In Figure 9, the time–frequency graphs of the fault and non-fault lines are different. Meanwhile, under high-resistance ground faults, although the zero-sequence current waveform difference between the faulty and non-faulty line is not obvious, after wavelet transform, these two types of data can be clearly distinguished. Therefore, using wavelet transform to conduct time–frequency analysis on zero-sequence current can effectively improve the detection accuracy.

A simulation model of a 10 kV small-current grounding system is built using the Matlab/Simulink simulation platform. Zero-sequence current data is obtained by setting different parameters. A total of 900 time–frequency diagrams of the simulation data are obtained. Some of the images are shown in Figure 10.

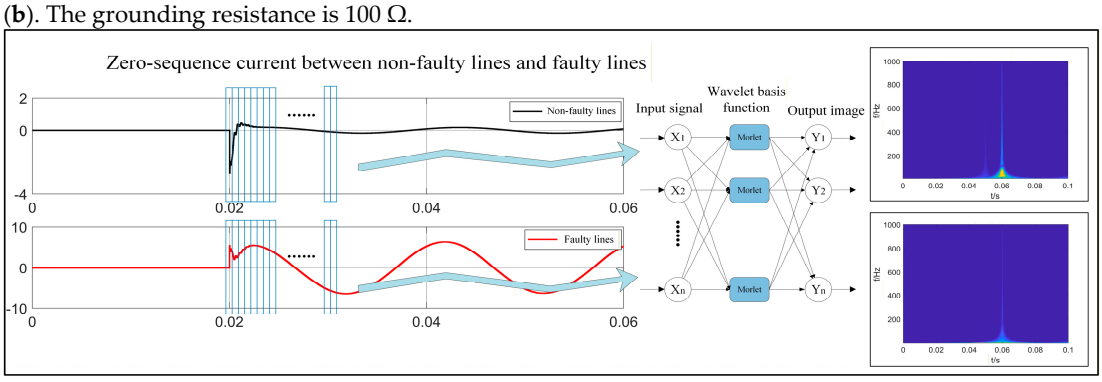
As can be seen from Figures 8 and 10, the frequencies of non-faulty lines are relatively high, all above 400 Hz, and some areas show the feature of high brightness. The frequency amplitudes of faulty lines are relatively low, generally below 400 Hz, and do not show the feature of local high brightness. Compared with the waveform data, the time–frequency diagram can be used to distinguish the faulty and non-faulty lines more intuitively.



(**a**). The grounding resistance is 10 Ω.

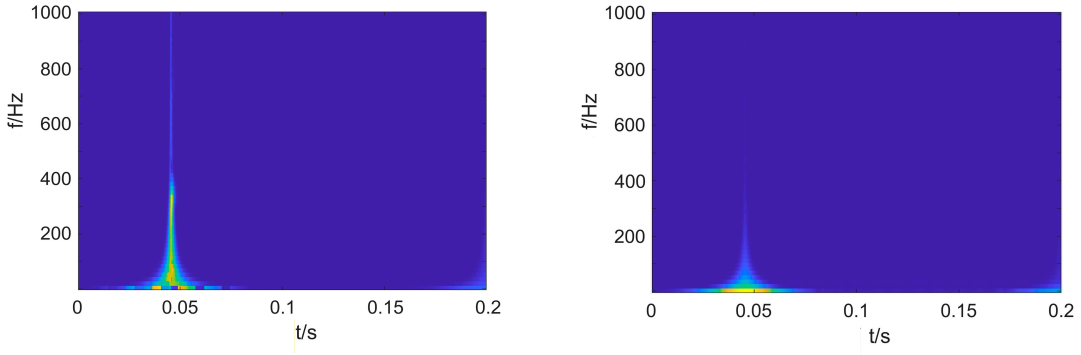


(**b**). The grounding resistance is 100 Ω.



(**c**). The grounding resistance is 300 Ω.

Figure 9. Zero-sequence current of the system and its wavelet transform under different grounding resistances.



(**a**) Non-faulty lines (**b**) Faulty lines

Figure 10. Time–frequency diagram of simulated data sample.

2.4.3. Dataset Composition Overview

To ensure the transparency of data sources and lay the foundation for the subsequent data splitting strategy, the detailed composition of the simulation and on-site datasets is explicitly specified as shown in Table 2:

Table 2. Dataset composition.

Dataset Type	Number of Unique Fault Events	Number of Unique Feeders	Total Samples (Time–Frequency Graphs)
Simulation Dataset	120	5	900
On-site Dataset	45	3	1800
Total Dataset	165 (120 simulation + 45 on-site)	8 (5 simulation + 3 on-site)	2700

2.5. Practical Deployment of Transfer Learning in TLM-Net

Combined with the TLM-Net network structure (MobileNet as the backbone, PAFPN + MFFN as the neck, and Decoupled Head + EKA as the detection head), the transfer learning in this study is deployed for the small-sample scenario of fault line selection (characterized by scarce on-site data and sufficient simulation data) through three core stages: source domain pre-training, backbone freezing, and target domain fine-tuning. The specific implementation process, frozen/fine-tuned modules and design rationale are elaborated as follows, and the overall deployment framework is consistent with the TLM-Net algorithm flow in Figure 1.

2.5.1. Pre-Training of the Source Domain Model

The source domain dataset is the 900 time–frequency graphs of zero-sequence current generated by the Matlab/Simulink simulation (covering different fault locations, grounding resistances and fault initial phases). We input the source domain dataset into the initial TLM-Net network (without MFFN and EKA modules, only the basic structure of MobileNet + PAFPN + Decoupled Head) for pre-training, with the training epoch set to 300, learning rate to 0.01 and momentum to 0.937. The goal of this stage is to make the backbone network learn the general fault feature prior knowledge of the zero-sequence current time–frequency graph and form a pre-trained source domain model with stable feature extraction capabilities.

2.5.2. Freezing of the Pre-Trained Backbone Network

To avoid overfitting of the model caused by the small size of the on-site target domain dataset, we freeze all the parameters of the pre-trained MobileNet backbone network in this stage. The frozen backbone network is used as a fixed feature extractor in the TLM-Net, which can retain the general fault feature extraction ability learned from the source domain simulation data and prevent the loss of pre-trained knowledge during the fine-tuning process of the small-sample target domain dataset.

2.5.3. Fine-Tuning of the Target Domain Model

The fine-tuning hyper-parameters are set as: the first 100 epochs with a learning rate of 0.01 (for fast adaptation of the improved modules to the target domain features), the last 200 epochs with a learning rate of 0.001 (for fine-grained optimization of network parameters), batch size of 32, and momentum of 0.937. The frozen backbone network provides fixed general fault features for the fine-tuned modules, and the fine-tuned modules learn the specific fault feature characteristics of the on-site target domain dataset, realizing the cross-domain adaptation of the feature space from the source domain (simulation data) to the target domain (on-site data).

3. Experimental Results and Analysis

3.1. Experimental Platform Configuration

The experimental environment, software and hardware configuration, and deep learning algorithm framework adopted are shown in Table 3.

Table 3. Configuration of the experimental platform.

Configuration	Version Parameter
Operating system	Windows10
GPU	NVIDIA GeForce RTX 3070
CPU	Intel Core i7-12700F@2.10 GHz
CUDA	11.7
Deep learning framework	pytorch

3.2. Analysis of Network Model Training and Experimental Results

Based on the YOLOv8 lightweight framework and the binary classification task characteristics of fault line selection, the core basic settings of the TLM-Net model are explicitly defined as follows:

(1) Base YOLOv8 Variant: TLM-Net is based on YOLOv8n, the lightweight variant of YOLOv8. This variant is selected for its small number of parameters and fast inference speed, which is highly adapted to the real-time engineering requirements of distribution network fault line selection.

(2) Input Resolution: The unified input resolution of the zero-sequence current time–frequency graph images is set to 640 × 512 pixels (W × H). This resolution is determined by the feature distribution characteristics of the time–frequency graph: it can fully retain the fine-grained frequency–time–amplitude feature information of the fault region (especially the low-frequency region below 400 Hz) without introducing excessive redundant pixel information.

(3) Label Format: Combined with the binary classification task (faulty/non-faulty lines) of this study and the fine-grained feature recognition requirement based on time–frequency graphs, a dual-label format is adopted for the dataset: primary label (whole-image classification label)—a one-hot vector label for binary classification—[1,0] for faulty line time–frequency graphs (positive class) and [0,1] for non-faulty line time–frequency graphs (negative class), which is the core label for the model's binary classification output; and auxiliary label (bounding-box label)—a rectangular bounding-box label (x_min, y_min, x_max, y_max) for the fault feature region in the time–frequency graph (coordinates normalized to [0,1]), which is used to assist the model in extracting fine-grained spatial features of the fault region (no impact on the final binary classification output, only for feature enhancement).

(4) Anchor Box Settings: The anchor boxes are designed based on the statistical characteristics of fault feature regions in 2700 time–frequency graphs (900 simulation + 1800 on-site). The original anchor scale of YOLOv8n is optimized and adapted to the time–frequency graph feature region, and the three-scale and three-aspect ratio anchor box settings are finally determined (the anchor sizes are normalized to the input resolution of 640 × 640): small scale—(10,13), (16,30), and (33,23)—for small fault feature regions (high grounding resistance and weak fault features); medium scale—(30,61), (62,45), and (59,119)—for medium fault feature regions (moderate grounding resistance); and large scale—(116,90), (156,198), and (373,326)—for large fault feature regions (low grounding resistance and obvious fault features). The anchor boxes are generated by the K-means clustering algorithm on the auxiliary bounding-box labels of the training set, which can be adaptively matched with the fault feature regions of different sizes in the time–frequency graph.

In the model performance evaluation stage, Mean Average Precision at IoU = 0.5 (mAP@0.5), precision rate k_{pre}, recall rate k_{re}, number of network parameters N_p, floating-point operation volume N_F, and detection speed are selected as evaluation indicators. All metrics are defined in accordance with the standard academic norms of deep learning and

binary classification tasks, and their standard definitions, calculation formulas and physical meanings in fault line selection are elaborated as follows.

3.2.1. Definition of Evaluation Metrics

Precision rate (k_{pre}): Also referred to as accuracy rate, it reflects the proportion of correctly identified positive samples in all samples predicted as positive samples, which measures the prediction accuracy of the model for fault/non-fault lines in this study.

Recall rate (k_{re}): Also referred to as sensitivity, it reflects the proportion of correctly identified positive samples in all actual positive samples, which measures the detection coverage of the model for faulty lines (the key target of line selection) in this study.

mAP@0.5 (Mean Average Precision at IoU = 0.5): The standard evaluation metric for object detection and fine-grained classification tasks, representing the mean value of the Average Precision (AP) for all categories at the Intersection over Union (IoU) threshold of 0.5. AP is calculated as the area under the precision–recall (P-R) curve for a single category, and mAP@0.5 is the mean of AP values for the faulty line and non-faulty line categories in this binary classification task of fault line selection.

3.2.2. Calculation Formulas and Notation Definition

For the binary classification task of distinguishing faulty lines (positive class, *P*) and non-faulty lines (negative class, *N*) in small-current grounding fault line selection, the core sample notations are defined as follows.

TP (True Positive): Actual faulty lines are correctly predicted as faulty lines (the key correct prediction for line selection); *TN* (True Negative): Actual non-faulty lines are correctly predicted as non-faulty lines; *FP* (False Positive): Actual non-faulty lines are incorrectly predicted as faulty lines (false alarm of fault); and *FN* (False Negative): Actual faulty lines are incorrectly predicted as non-faulty lines (missed detection of fault).

The calculation formulas for the metrics are as follows:

$$k_{pre} = \frac{TP}{TP + FP} \tag{11}$$

$$k_{re} = \frac{TP}{TP + FN} \tag{12}$$

$$AP = \int_0^1 P(R)dR,\ mAP@0.5 = \frac{1}{C}\sum_{i=1}^{c} AP_i \tag{13}$$

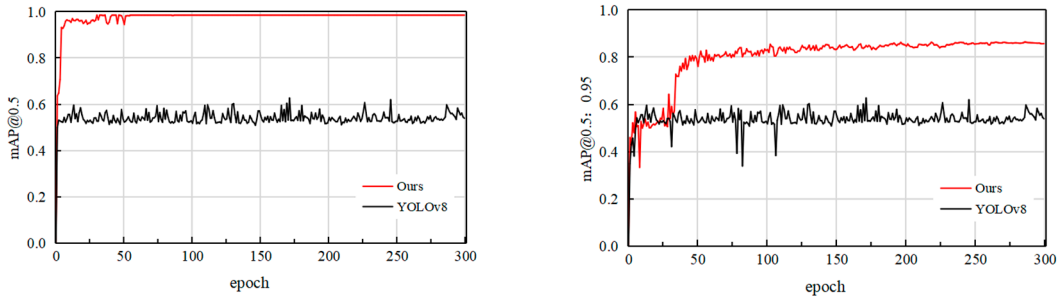
P (R) is the precision–recall (P-R) curve function for a single category, with recall (R) as the independent variable and precision (P) as the dependent variable; C = 2 is the number of categories in this study (faulty line and non-faulty line); and AP_i is the Average Precision of the i-th category, calculated as the area under the P-R curve of the i-th category at the IoU threshold of 0.5.

3.2.3. Results and Analysis of Ablation Experiments

(1) Analysis of model training results

To objectively evaluate the detection performance, TLM-Net is compared with the YOLOv8 detection framework. The training results are shown in Figure 11.

It can be seen from Figure 11 that the mAP@0.5 and mAP@0.5:0.95 of TLM-Net are significantly higher than YOLOv8. The mAP@0.5 of TLM-Net stabilized at around 0.985 finally. The mAP@0.5 of YOLOv8 hovered around 0.55, with an average of around 0.61.



(**a**) mAP@0.5 (**b**) mAP@0.5:0.95

Figure 11. The mAP@0.5 curve and the mAP@0.5:0.95 curve.

(2) Analysis of improved module ablation results

As the MFFN and EKA are designed, the ablation experiments are conducted to verify the functions of each module, as shown in Table 4.

Table 4. Results of the ablation experiment.

Transfer Learning	MFFN	EKA	mAP@0.5/%	N_P/B	N_F/GFLOPs	k_{pre}/%	k_{re}/%	Speed/ms	Weight/KB
			61.0	3,009,782	8.2	89.5	91.3	12.3	23,953
√			75.7	3,009,782	8.2	91.2	90.6	12.5	24,925
	√		72.2	3,115,519	8.8	90.1	91.6	15.6	30,806
√	√		92.8	3,115,904	8.8	92.6	89.7	15.6	32,302
		√	71.9	3,112,703	8.2	91.8	92.0	12.4	24,978
√		√	87.8	3,012,703	8.2	95.3	89.2	12.4	24,782
	√	√	88.5	3,115,519	8.8	96.3	89.2	16.8	31,462
√	√	√	98.5	3,126,786	8.8	98.3	96.5	16.6	31,978

When only the transfer learning module is added to the base framework, the model's mAP@0.5 reaches 75.7%, which is significantly higher than the base framework. This result verifies that the transfer learning strategy of pre-training on simulation data and fine-tuning on on-site data effectively solves the problem of low model accuracy caused by scarce on-site fault samples (small-sample scenario). By transferring the general fault feature prior knowledge learned from the source domain (simulation data) to the target domain (on-site data), the model's generalization ability is significantly improved, and the feature extraction ability for on-site weak fault features is enhanced without increasing the model's complexity.

When only the MFFN is added, the model's mAP@0.5 reaches 72.2%, and the precision/recall rates are 90.1%/91.6%. The slight increase in N_P and N_F is due to the three-branch feature fusion structure of the MFFN. This improvement indicates that the MFFN effectively makes up for the deficiency of the original PAFPN in multi-scale feature interaction, and realizes the synergistic extraction of global context information and local detail features of fault time–frequency graphs, thus enhancing the model's ability to capture multi-scale fault features.

When only EKA is added, the model's mAP@0.5 reaches 71.9%, with precision/recall rates of 91.8%/92.0%. The EKA module (integrating AKConv) realizes adaptive multi-region feature focusing and suppresses background noise interference in time–frequency graphs, which significantly improves the model's recognition accuracy for irregular weak fault feature regions and the saliency of fault target regions, thus achieving performance improvement without obvious increase in model complexity.

When transfer learning, the MFFN and EKA are integrated, the model achieves optimal comprehensive performance: mAP@0.5 = 98.5%, precision rate = 98.3%, and recall rate = 96.5%. Compared with the single transfer learning module, the mAP@0.5 is increased by 37.5%, and the precision/recall rates are increased by 8.8% and 5.2%, respectively. The model's N_P and N_F only increase slightly, and the detection speed still meets the real-time engineering requirements of distribution network fault line selection. This optimal performance reflects the triple synergistic enhancement mechanism of the three core modules: (1) transfer learning solves the small-sample problem of on-site data and provides general fault feature prior knowledge; (2) the MFFN fuses global and local multi-scale fault features based on prior knowledge, realizing cross-level semantic complementarity; (3) and EKA further strengthens the recognition of weak and irregular fault features and suppresses background noise, realizing the precise extraction of fault features.

3.2.4. Comparative Experiments

To ensure a fair, objective, and reproducible performance comparison, the baseline methods are selected according to the following principles: Representativeness—Cover classical fault detection methods and mainstream deep learning detection models. Universality—Use publicly available, widely recognized, and commonly adopted algorithms rather than highly customized methods from individual references. Technical coverage—Include methods based on traditional features, generic deep learning, and attention-enhanced networks.

In comparative experiments, TLM-Net is compared with Faster-RCNN, SSD, EfficientDet, CenterNet, YOLOv5, SE-YOLOv5, YOLOv8 and SE-YOLOv8, as shown in Table 5. The comparison curves of mAP@0.5 are shown in Figure 12.

Table 5. The results of comparative experiments.

Algorithm	mAP@0.5/%	N_P/ B	N_F/GFLOPs	k_{pre}/%	k_{re}/%	Speed/ms
Faster-RCNN [18]	81.4	29,653,729	78.12	38.6	49.0	73.1
SSD [19]	41.8	23,678,263	137.07	45.9	80.1	21.5
EfficientDet [20]	81.1	72,055,668	6.1	70.3	42.8	35.0
CenterNet [21]	87.0	25,517,032	142.13	53.3	73.6	15.8
YOLOv5	55.7	7,015,519	15.8	87.6	91.3	14.9
SE-YOLOv5	75.3	7,057,791	13.0	88.8	89.3	15.6
YOLOv8 [22]	61.0	3,009,782	8.2	89.5	91.3	12.3
SE-YOLOv8	77.6	3,011,129	8.2	89.6	89.7	12.9
TLM-Net	98.5	3,126,786	8.8	98.3	96.5	16.6

Faster-RCNN and SSD adopt the traditional feature extraction and fusion structure, which lacks the targeted design for the multi-scale and weak characteristics of fault features in time–frequency graphs. TLM-Net optimizes the network structure by adding MFFN and EKA modules, which realizes the synergistic extraction and enhancement of multi-scale fault features, and thus has a stronger feature extraction ability than the classic algorithms. All comparison algorithms are trained directly on the on-site small-sample dataset without the transfer learning strategy, which leads to poor generalization ability and low detection accuracy of the models. TLM-Net adopts the transfer learning strategy of pre-training on simulation data, which makes full use of the rich fault feature information of simulation data and effectively solves the small-sample problem of on-site data, thus achieving significant performance improvement compared with the comparison algorithms. The two-stage detection algorithm Faster-RCNN has a high detection accuracy but large number of parameters and slow inference speed, which cannot meet the real-time requirement of distribution network fault line selection; the lightweight algorithm SSD has a fast inference

speed but low detection accuracy for weak fault features; and YOLOv5 and YOLOv8 have a good balance between accuracy and real-time performance, but lack the targeted optimization for the weak fault feature recognition and small-sample adaptability. TLM-Net is optimized on the basis of YOLOv8n, and while improving the detection accuracy, it maintains the lightweight and real-time characteristics of the model, which is more suitable for the practical engineering application scenario of small-current grounding fault line selection. Most comparison algorithms are general object detection/classification algorithms, which are not designed for the specific task of small-current grounding fault line selection. TLM-Net combines the characteristics of the fault line selection task to design the core modules, and converts the fault line selection task into a fine-grained binary classification task based on time–frequency graphs, which makes the model better adapted to the specific task and thus achieves higher detection accuracy.

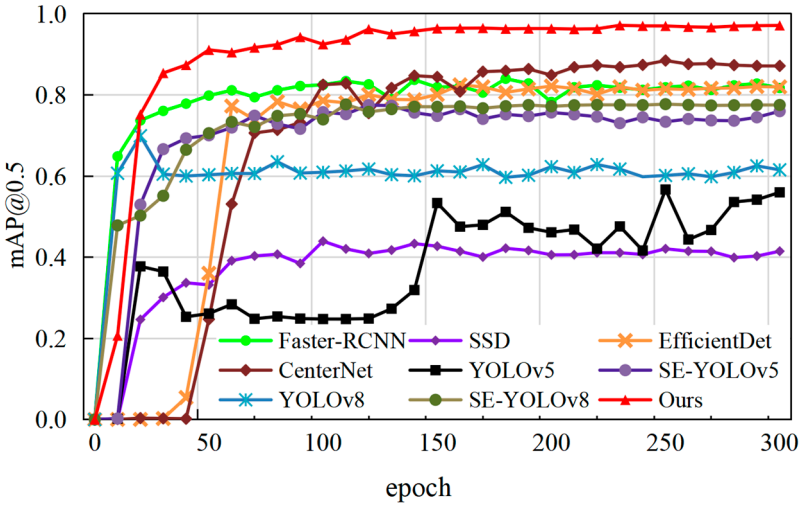


Figure 12. Comparison curves of mAP@0.5.

4. Conclusions

Aiming at the issue of the low efficiency of multi-scale feature fusion in traditional algorithms, a novel line selection method based on transfer learning is proposed.

(1) By pre-training the source domain model through simulation data and combining it with the knowledge transfer mechanism, the problems of low algorithm accuracy and poor robustness under the condition of small samples have been effectively alleviated.
(2) The designed multi-scale feature fusion network enhances the model's ability to represent complex features through the collaborative extraction of global and local information.
(3) The EKA mechanism that fuses variable kernel convolution is introduced, which not only suppresses background noise but also improves the detection accuracy of irregular targets.

The final experiment shows that the mAP@0.5 of TLM-Net reaches 98.5%, which is 37.5% higher than that of the original YOLOv8, and both the accuracy and recall rates are superior to the comparison algorithms. Although the number of model parameters and the amount of computation have slightly increased, its performance advantages in weak feature extraction and high-precision line selection scenarios are significant. When comparing the TLM-Net algorithm with eight classic detection algorithms, the TLM-Net line selection method has significant advantages.

Author Contributions: Conceptualization, L.L. and S.H.; methodology, L.L. and S.H.; validation, L.L. and W.W.; investigation, L.L.; resources, L.L. and S.H.; data curation, L.L. and W.W.; writing—original

draft preparation, L.L. and W.W.; writing—review and editing, L.L. and S.H.; visualization, L.L.; supervision, L.L. and S.H.; project administration, L.L.; funding acquisition, L.L. All authors have read and agreed to the published version of the manuscript.

Funding: This work was funded by the National Natural Science Foundation of China, grant number 52574264.

Institutional Review Board Statement: Not applicable.

Informed Consent Statement: Not applicable.

Data Availability Statement: The data presented in this study are available on request from the corresponding author due to privacy.

Conflicts of Interest: The authors declare no conflicts of interest.

References

1. Yang, D.; Lu, B.; Lu, H. High-Resistance Grounding Fault Detection and Line Selection in Resonant Grounding Distribution Network. *Electronics* **2023**, *12*, 4066. [CrossRef]
2. Shen, Q. A novel method of fault line selection in low current grounding system using multi-criteria information integrated. *Electr. Power Syst. Res.* **2022**, *209*, 108010. [CrossRef]
3. Yang, F.; Li, H.; Hu, W. Identification of Single-Phase Line Break Fault Direction Based on Local Voltage Information in Small Current Grounding System Considering the Impact of DG. *IEEE Access* **2023**, *11*, 120754–120765. [CrossRef]
4. Liu, P.; Huang, C. Detecting Single-Phase-to-Ground Fault Event and Identifying Faulty Feeder in Neutral Ineffectively Grounded Distribution System. *IEEE Trans. Power Deliv.* **2018**, *33*, 2265–2273. [CrossRef]
5. Jin, W.; Zhang, S.; Zhao, J. Dynamic Time Warping-Based Differential Protection Scheme for Transmission Lines in Flexible Fractional Frequency Transmission Systems. *Electronics* **2025**, *15*, 45. [CrossRef]
6. Su, S.; Xie, Q.; Ma, P. A Single-Phase Ground Fault Line Selection Method in Active Distribution Networks Based on Transformer Grounding Mode Modification. *Energies* **2024**, *17*, 4743. [CrossRef]
7. Wan, G.; Xu, X. Research on single-phase grounding detection method in small-current grounding systems based on image recognition. *Front. Energy Res.* **2024**, *12*, 1473472. [CrossRef]
8. Zhou, Y.; Liu, K.; Ding, W. Neutral-Point Voltage Regulation and Control Strategy for Hybrid Grounding System Combining Power Module and Low Resistance in 10 kV Distribution Network. *Electronics* **2024**, *13*, 3608. [CrossRef]
9. Tian, J.; Jiang, L.; Li, H. A method of single-phase grounding fault line selection based on optimization spiking neural P systems. *Front. Energy Res.* **2022**, *10*, 981404. [CrossRef]
10. Wang, P.; Xu, B.; Wang, C. Protection method for high-impedance grounding fault in neutral isolated system based on comparative phase analysis of fault phase voltage and zero-sequence current. *Electr. Power Autom. Equip.* **2024**, *44*, 148–156.
11. Jiang, B.; Dong, X.; Shi, S. Experimental research on typical single-phase grounding line selection methods of distribution network. *Electr. Power Autom. Equip.* **2015**, *35*, 67–74.
12. Li, G.; Pan, M.; Liu, Y. Research on Line Selection Method and Analysis of Small Grounding Fault Simulation. *Electr. Eng.* **2022**, *8*, 145–148.
13. Su, X.; Zhang, H.; Gao, Y. The classification model for identifying single-phase earth ground faults in the distribution network jointly driven by physical model and machine learning. *Front. Energy Res.* **2023**, *10*, 919041. [CrossRef]
14. Cheng, W.; Xu, M.; Gao, J. Spatial domain image generation and fusion method of single-phase grounding fault line selection for small current grounding system. *Electr. Power Autom. Equip.* **2021**, *41*, 97–103.
15. Lilly, J.; Olhede, S. On the analytic wavelet transform. *IEEE Trans. Inf. Theory* **2010**, *56*, 4135–4156. [CrossRef]
16. Ouyang, D.; He, S.; Zhang, G. Efficient multi-scale attention module with cross-spatial learning. In *Proceedings of the ICASSP 2023—2023 IEEE International Conference on Acoustics, Speech and Signal Processing (ICASSP), Rhodes Island, Greece, 4–10 June 2023*; IEEE: Piscataway, NJ, USA, 2023; pp. 1–5.
17. Zhang, X.; Song, Y.; Song, T. AKConv: Convolutional kernel with arbitrary sampled shapes and arbitrary number of parameters. *arXiv* **2023**, arXiv:2311.11587. [CrossRef]
18. Ren, S.; He, K.; Girshick, R. Faster R-CNN: Towards real-time object detection with region proposal networks. *IEEE Trans. Pattern Anal. Mach. Intell.* **2016**, *39*, 1137–1149. [CrossRef] [PubMed]
19. Liu, W.; Anguelov, D.; Erhan, D. Ssd: Single shot multibox detector. In *Computer Vision European Conference*, 14th ed.; Springer: Cham, Switzerland, 2016; pp. 21–37.
20. Tan, M.; Pang, R.; Le, Q. Efficientdet: Scalable and efficient object detection. In *Proceedings of the IEEE/CVF Conference on Computer Vision and Pattern Recognition, Seattle, WA, USA, 13–19 June 2020*; IEEE: Piscataway, NJ, USA, 2020; pp. 10781–10790.

21. Duan, K.; Bai, S.; Xie, L. Centernet: Keypoint triplets for object detection. In *Proceedings of the IEEE/CVF International Conference on Computer Vision, Seoul, Republic of Korea, 27–28 October 2019*; IEEE: Piscataway, NJ, USA, 2019; pp. 6569–6578.
22. Varghese, R.; Sambath, M. Yolov8: A novel object detection algorithm with enhanced performance and robustness. In *2024 International Conference on Advances in Data Engineering and Intelligent Computing Systems (ADICS), Chennai, India 18–19 April 2024*; IEEE: Piscataway, NJ, USA, 2024; pp. 1–6.

Disclaimer/Publisher's Note: The statements, opinions and data contained in all publications are solely those of the individual author(s) and contributor(s) and not of MDPI and/or the editor(s). MDPI and/or the editor(s) disclaim responsibility for any injury to people or property resulting from any ideas, methods, instructions or products referred to in the content.